CrossMark

Relating Interface Evolution to Interface Mechanics Based on Interface Properties

DEVENDRA VERMA,[1] SUDIPTA BISWAS,[1] CHANDRA PRAKASH,[1]
and VIKAS TOMAR[1,2]

1.—School of Aeronautics and Astronautics, Purdue University, West Lafayette, IN 47907, USA.
2.—e-mail: tomar@purdue.edu

The current article focuses on recent work done in understanding the role of processing techniques on interface evolution and connecting interface evolution to interface thickness-dependent properties. Special emphasis is placed on interface evolution during the sintering process of tungsten (W). Sintering with additives such as nickel significantly changes grain boundary properties in W, leading to issues such as grain boundary embrittlement. When one has to mechanically describe properties of polycrystalline W with an account of the influence of grain boundary embrittlement, one must explicitly consider grain boundary properties. This issue is the focus of the present work on the mechanical properties of interfaces. Overall, a phase field modeling-based approach is shown to be an excellent computational tool for predicting the interface evolution. The influences of the interface thickness, chemistry, and orientation of phases around interfaces are analyzed using extended finite element simulations for polycrystalline W.

INTRODUCTION

Interfaces are ubiquitous entities present in polymer composites, metals, ceramics, and biomaterials.[1–8] Interfaces are usually found at a length scale of micrometers in composite materials (usually characterized as interphases) and at a length scale of nanometers in metals (usually characterized as grain boundaries; GBs). In the case of metals, microstructural changes including phase transformation, grain growth, etc. are governed significantly by the interfacial chemistry, interface width (saturated versus unsaturated interfaces),[9,10] and interface energy. Consequently, interface properties also significantly affect mechanical deformation of materials. For example, in situ transmission electron microscopy (TEM) experiments performed on Al-TiN multilayers by Mara et al.[11] demonstrated the size effect related to plastic co-deformation of layers in multilayer materials. The interface evolution as a wavy structure with corners and facets in roll-bonded metallic materials has been illustrated via mesoscale thermodynamic modeling.[12] Interfaces have also been shown to interact with material defects and dislocations eventually affecting their evolution. The interface role as a sink to absorb point defects and nucleate dislocations in a Cu/Nb multilayered composite material with high interfacial content was studied by Wang et al.[13] The possible application of interfaces to alter the role of dislocation slip and twinning was suggested through atomistic simulations by Mara et al.[14] Interfaces are considered to play a key role in the reduction of radiation damage in nuclear materials.[15] Interfaces in the metal matrix composites were studied by Weng et al.,[16] exhibiting the importance of interface morphology on mechanical properties. Transition of mechanical properties across solid–solid interfaces has been studied by Srinivasan et al.[17] using TEM and atom probe tomography (APT). Properties of interface-dominated materials such as nano-layered crystalline composites were modeled using a multiscale analysis-based approach by Wang et al.[18] Bulk-scale properties of a material have been found to have a profound effect on interface properties.[19] Growth of the intermetallic layers between two dissimilar materials has been modeled by Dybkov.[20] Gupta et al.[21] analyzed the diffusion of individual layers through interfaces in multilayered materials in the case of aluminum laminates. Dynamic crack propagation in a material with inclusions has been

experimentally studied and shown to be affected by interface strength,[22,23] as well as by the interface inclination angle.[24]

As discussed so far, interfaces have immense potential to redefine the design principles of next generation materials. Experimental methods, used in the characterization of interfaces, e.g., Focused Ion Beam (FIB) in compression testing Refs. 25–27 or micro-/nano-indentation Refs. 3, 28, and 29 have limitations in the applicability for different materials and interfaces at multiple length scales. Due to this issue, alternatives are sought and computational methods serve as an excellent tool. The current article focuses on recent work done in understanding the role of processing on interface evolution, and on connecting interface evolution to interface thickness-dependent properties.

INTERFACE EVOLUTION STUDIES

Interfaces have been shown to play a significant role in new manufacturing techniques such as additive manufacturing.[30] Interface formation and its impact on material behavior has been studied for different manufacturing and material processing techniques such as sintering, annealing, etc. Sintering is an age-old processing method in powder metallurgy involving the compaction of powder particles into a solid structure. It is a manufacturing technique which creates a solid polycrystalline structure from small powder particles with reduced surface area and improved density. During the sintering process, the curvature of the interface reduces and flat GBs are created. Microstructural evolution in this case is governed by diffusion across the interface.

Interface modeling and strength prediction is a multiscale phenomenon. Various mesoscale approaches used to model interface evolution include: PFM simulations, cellular automata simulations, and kinetic Monte Carlo simulations. Cellular automata assumes a single grain or sub-grain to be a representative segment of a microstructure. Hence, it fails to consider the impact of interface geometries and properties on microstructural changes. On the other hand, kinetic Monte Carlo simulation represents the microstructure with the collection of discrete points that are generated randomly and then the observing of microstructural alterations by quantifying the changes in the discrete grid points. This method is highly stochastic in nature and does not model physical interfaces.[31] PFM can replicate physical microstructures with specific grain orientations and interfacial structures. In the case of PFM simulations, interface behavior is mainly modeled based on sharp interface and diffuse interface models. Both the models identify each phase using unique order parameters. However, the models differ in their approach to observing interface evolution. The sharp interface model requires tracking of the tip velocity of the interface, whereas the diffuse interface model predicts the interface behavior by observing the evolution of a continuous PFM variable without physically tracking the interface. The current work uses the diffuse interface model to capture the interface evolution and microstructural changes during sintering.

PFM is an effective tool for simulating microstructural evolution at the mesoscale. For decades, PFM has been applied to predict the impact of different material processing techniques, including but not limited to diffusion,[32] solidification,[33–35] solid-state phase transformation,[36,37] translation of defects and dislocations,[38–41] grain growth,[42,43] and crack propagation.[44,45] In this method, the microstructure is assumed to be a thermodynamically unstable structure which evolves in time and space trying to achieve equilibrium by minimizing the free energy. The microstructural features such as concentration of phases, grain orientation, etc. are considered as PFM variables. Here, the evolution of the phases, the shape of the grains, and the positions of the interfaces are implicitly set by the evolution of the phase-field variables. It can consider several thermodynamic factors simultaneously, leading to microstructural changes such as bulk and interfacial energy, elastic energy, electric or magnetic energy, etc. At the same time, it can take into account different transport mechanisms such as mass diffusion, heat conduction and convection.[46] PFM denotes interface evolution and alterations in microstructure by capturing the numerical changes in assigned PFM variables. The equations for the evolution of phase-field variables are derived based on general thermodynamic principles.[46] The total free energy, F, is expressed as a function of conserved and non-conserved variables that varies with time and spatial coordinates. Usually, conserved variables represent the concentration or volume fraction of a certain phase in the whole material system and non-conserved variables separately identify co-existing phases. The total free energy is generally represented as,

$$F = \int \left[f_0(c,\eta) + f_{ex}(c,\eta) + \frac{\kappa_c}{2} |\nabla c|^2 + \frac{\kappa_\eta}{2} |\nabla \eta|^2 \right] dV$$

(1)

where $f_0(c, \eta)$ is the bulk free energy of the material that determines the volume fraction of the phases at equilibrium condition, $f_{ex}(c, \eta)$ is the energy contribution due to external energy field, and κ_c and κ_η are the gradient coefficients corresponding to conserved variable, c, and non-conserved order parameter, η, respectively.[46] The 3rd and 4th terms in Eq. 1 denote the gradient free energy from the interfaces. Two major components of the total free energy are the bulk free energy and the gradient energy terms. Bulk free energy is the chemical free energy inherited by the material due to its constituent phases. This can be obtained from

molecular dynamics or quantum simulations. Thermodynamic tools like CALPHAD can also be used to generate phase diagrams and derive the chemical free energy of a multi-phase system depending on the concentration of each phase in the system. Bulk free energy is designed to be minimum inside a phase, but maximum at the interface. It dominates the equilibrium phase concentration of the system. Gradient free energy, on the other hand, determines the interface evolution during phase transformation and dictates changes in the shape of the grains required to achieve equilibrium. Additional energies are taken into account when external mechanical, thermal, electric or magnetic fields are present during the phase transformation process. Here, the interfaces evolve with time to minimize the total free energy, thus leading to microstructural evolution. In PFM, the temporal evolution of the phase-field variables is governed by a set of coupled partial differential equations, one equation for each variable. The equations are derived according to the principles of non-equilibrium thermodynamics. They are formulated in such a way that the total free energy decreases monotonically. Solution of the partial differential equations yields the temporal and spatial evolution of the phase-field variables, which represent the morphological alterations of the interface and the material microstructure. The Cahn–Hilliard (CH) equation Ref. 47 is used to track the conserved concentration field(c) as,

$$\frac{\partial c}{\partial t}(\vec{r}, t) = \nabla \cdot \left[M\nabla \frac{\delta F}{\delta c} \right] \quad (2)$$

Similarly, the evolution of the non-conserved order parameter (η_i) is defined using the Allen–Cahn (AC) equation as,

$$\frac{\partial \eta_i}{\partial t}(\vec{r}, t) = -L\nabla \frac{\delta F}{\delta \eta_i} \quad (3)$$

where F is the total free energy of the system as defined in Eq. 1 earlier, parameter M is the diffusion mobility, parameter L is the GB mobility due to atomic jump across the interface, and suffix i represents the number of the order parameter. Multiple non-conserved order parameters are used in the simulation, each uniquely associated with single particle representing its grain orientation. Each particle is assumed in this case to be a single crystalline; multi-grain particles will be part of future studies.

Gradient energy coefficients and the interface mobility of a material impacts the interfacial evolution. Interfacial energy is defined as the excess energy in the interface region of the material. Considering the equilibrium condition, the equilibrium interface thickness can be obtained from Eqs. 2 and 3 using the gradient energy co-efficient. Qin and Bhadeshia[48] has shown the derivation of the equilibrium interface thickness for conserved phase-field variables. The interface thickness, δ, is usually estimated as $\delta = 4\kappa\sqrt{2\omega}$ a function of a gradient co-efficient, κ, and an interface fitting parameter, ω. In PFM, the initial interface thickness is provided as an input to the simulation, and, as the microstructure evolves, the interface reaches its equilibrium thickness. Mobility, calculated from the diffusion coefficients, is defined as,

$$M = M_{vol}\phi(c) + M_{vap}[1 - \phi(c)] + M_{surf}c(1 - c)$$
$$+ M_{gb}\sum_i \sum_{j \neq i} \eta_i\eta_j \quad (4)$$

where $\phi(c) = c^3(10 - 15c + 6c^2)$ and M_{vol}, M_{vap}, M_{surf}, and M_{gb} are the coefficients for atomic mobility in solid bulk, vapor, along the surface and GB phases, respectively.[49] Parameters η_i and η_j represent the order parameters connected to the ith and jth particles, respectively. The overall mobility expression is designed in such a way that each diffusion mechanism is active in the corresponding region of interest. For example, M_{vol} and M_{vap} are only active in the particle and void phases, respectively. Similarly, M_{surf} acts at the interface between two co-existing phases (particle and void phase) and M_{gb} dominates in this case at the interface between two particles, the same as the grain boundaries,. The polynomial expression used for ϕ is the same as the higher order switching function expression used for the physical property representation of any multi-phase system. Mobility co-efficients (M_i) are estimated according to the work of Moelens et al.[46] from corresponding diffusion co-efficients as,

$$M_i = \frac{D_i V_m}{k_B T} \quad (5)$$

Here, D is the diffusion co-efficient and suffix i corresponds to volume, vapor, GB and surface diffusion, V_m is the molar volume, k_B is the Boltzman constant, and T is the absolute temperature. The diffusion co-efficients can be expressed as a function of temperature (T) and activation energy (Q_i) values as,

$$D_i = D_{i0} \exp\left(\frac{-Q_i}{k_B T}\right) \quad (6)$$

Here, D_{i0} is the diffusion prefactor used for diffusivity calculations. Diffusivity prefactors and activation energies for the diffusion of a material at a certain temperature have usually been derived from experimental data.[50–52] Table I represents the coefficients of self-diffusion for W.

The difference in the reported values can be attributed to the differences in experimental techniques, sample preparation, impurities, etc. Table II shows the diffusivity values and mobilities calculated for W at 1200 K temperature.

Table I. Self-diffusion in tungsten; Mundy and Neumann have expressed diffusion co-efficients as a summation of two exponential functions, and the prefactors and activation energies corresponding to both the functions are reported here (rows 3 and 4)

D_0 (10^{-4} m^2 s^{-1})	Q (eV)	T-range (K)	References
1.88	6.084	2073–2676	Pawel[53]
15.3	6.487	2042–2819	Arkhipova[54]
46 and 0.04	6.9 and 5.45	1705–3409	Mundy[51]
200 and 0.13	7.33 and 5.62	1705–3409	Neumann[55]

Table II. Mobility calculation for tungsten

GB mobility[50]			Surface mobility[52]			Volume mobility[51]		
Diffusion prefactor (cm/s^2)	Activation energy (ev)	Mobility (μm^5/ev s)	Diffusion prefactor (cm/s^2)	Activation energy (ev)	Mobility (μm^5/ev s)	Diffusion prefactor (cm/s^2)	Activation energy (ev)	Mobility (μm^5/ev)
0.141	3.04	3.69×10^{15}	4.0	3.14	3.9869×110^{15}	0.04	5.4	1.29569×110^4

Interface geometry and its properties impact the gradient energy coefficients. The gradient energy coefficients, i.e. κ values, can be calculated when the interfacial energy and interface thickness of the materials are known,

$$\kappa_c = k_1(2\gamma_s - \gamma_{GB})\delta, \quad \text{and} \qquad (7)$$

$$\kappa_\eta = k_2\gamma_{GB}\delta \qquad (8)$$

Here, γ_s and γ_{GB} are the surface and GB energy, respectively and δ is the interface width, and k_1 and k_2, are the constants used for normalizing the material parameters. Changes in the GB and surface energy ratio impact the gradient parameters, which eventually affect the microstructural evolution. Biswas et al.[56] have studied the effect of the surface energy to GB energy ratio during sintering. The neck length variation corresponding to two different energy ratio values is shown in Fig. 1a. The energy ratio (γ_s/γ_{gb}) is controlled by changing the κ values, which, in turn, represent variation in the interfacial properties. This primarily impacts the initial sintering stage when neck formation is dominated by surface diffusion. Higher energy ratios indicate higher surface energy values and higher interfacial energy coefficient values, which lead to faster diffusion at the initial stage. The rate of densification increases with the increase in energy ratio. Also, the time to reach final neck length decreases with the increase in energy ratio.

Figure 1b shows that, as the energy ratio increases, the rate of grain growth also increases and the average grain size decreases for the initial few seconds and starts gradually increasing thereafter. This happens due to different interface and bulk behavior at different stages of the process. At the initial stage, interface thickness reduces due to surface diffusion as the interface tries to attain its equilibrium thickness, resulting in a decrease in individual grain sizes. At later stages, as particles start interacting with each other, overall grain size increases due to bulk diffusion. The diffusion mechanisms and changes in different interfaces leading to overall microstructural evolution are shown in Fig. 2.

Interfacial properties are known to affect the equilibrium microstructural configuration. The dihedral angle between adjacent grains is determined by the GB to surface energy ratio, mobility and interfacial parameters. The equilibrium dihedral angle is defined as;

$$\varphi = 2\cos^{-1}\left(\frac{\gamma_{GB}}{2\gamma_s}\right) \qquad (9)$$

where φ is the dihedral angle between grains at the neck location and γ_{GB} and γ_s are the GB energy and surface energy, respectively. Different energy ratios yield different equilibrium dihedral angles. Higher energy ratios correspond to higher dihedral angles that eventually governs the final neck length and grain configuration. Higher grain growth rates indicate that the densification is governed by volumetric bulk diffusion. The grain growth mechanisms can be identified from quantifying the change in grain size,

$$G^n(t) - G_0^n = kt \qquad (10)$$

where $G(t)$ is the average grain size at time t, G_0 is the average initial grain size, and k is the rate constant. The value of the growth exponent (n) is dictated by the predominant diffusion mechanism. A relationship of the grain growth exponent to the diffusion mechanism was shown in the authors' previous work.[56] Overall, PFM serves as a
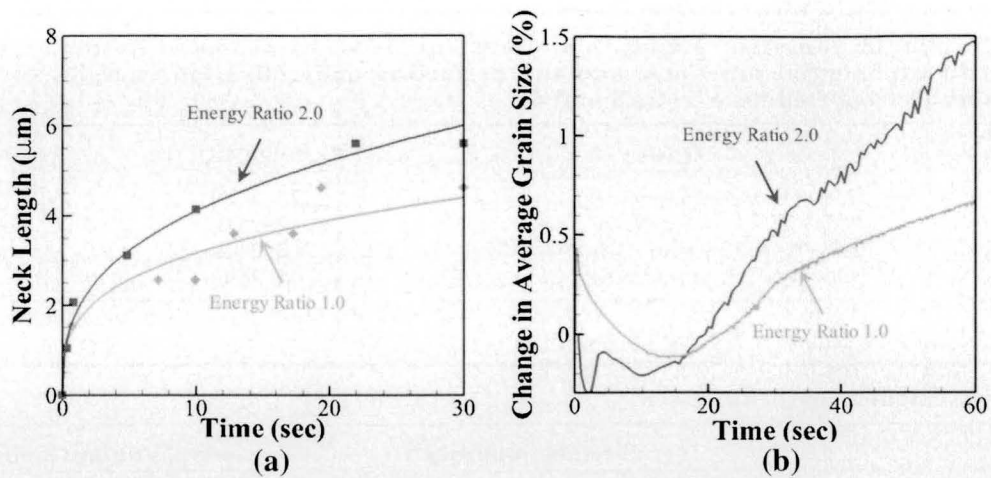
Fig. 1. (a) Neck length variation corresponding to different energy ratios,[35] and (b) effect of energy ratio on grain growth rate of particles during sintering.
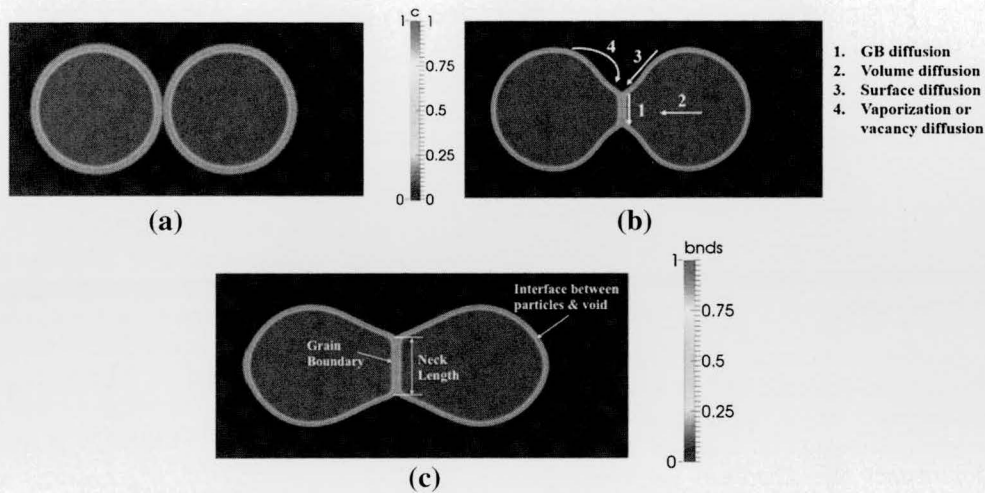

Fig. 2. Interface evolution during sintering; (a) initial particle configuration; (b) diffusion mechanisms leading to microstructural changes; (c) neck growth and grain boundary formation during sintering.

promising simulation technique to predict the influence of interface properties in a manufacturing process such as sintering. These prediction capabilities can be utilized to customize the materials with a user-defined interface density which will give it the properties based on the application, such as energetic magnetic materials.

INTERFACE MECHANICAL PROPERTIES

In the case of metals, microstructural changes including phase transformation, grain growth, etc. are governed significantly by the interfacial chemistry, interface width (saturated versus unsaturated interfaces),[9,10] and interface energy. Research has shown that the interface saturation level during sintering changes the average interface width which leads to interfaces having thickness- and chemistry-

dependent cohesion and strength properties.[9,10,57] The saturation level also affects interface elastic constant values and is directly related to phenomena such as GB embrittlement.[58] Based on these findings, Lee et al.,[59] examined GB embrittlement in polycrystalline W and derived a new embrittlement parameter that relates to chemistry and mechanical strength of GBs, which can be derived based on images of specimen fracture using a failure index criterion derived in the same work. The finite element simulation model (Fig. 3b) is constructed based on the image of a realistic Ni-doped W GB from a HRTEM image[58] (Fig. 3a), resulting in an interface structure. Crack propagation was modeled using XFEM and the interface was modeled using a surface-based cohesive zone model in ABAQUS.[60] Interface properties were given in terms of a bilinear traction–separation law.[59]
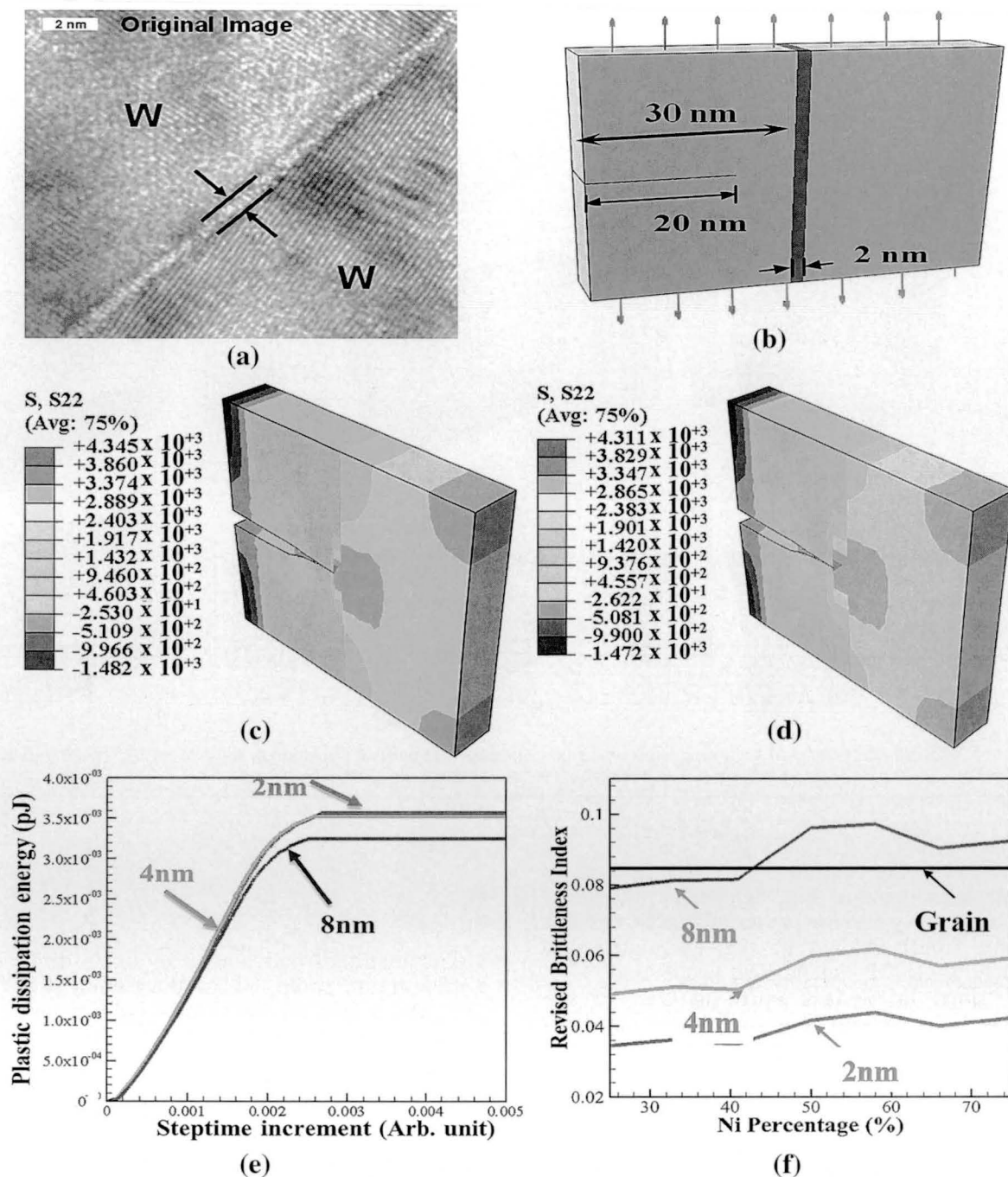
Fig. 3. A schematic showing (a) HRTEM image of polycrystalline Ni-doped W GB (reprinted with permission from 58), (b) finite element model analyzed for crack propagation; stress distribution when the crack tip reaches the interface for, (c) 2 nm, (d) 4 nm GB thickness; (e) plastic dissipation energy with time increment; (f) revised brittleness index for all three GB thickness as a function of Ni percentage (reprinted with permission from 59). Straight black line represents respective average brittleness index for grains.[9,10]

The effect of chemistry dependent interface strength calculated using quantum mechanical ab initio simulations on polycrystalline W fracture resistance was quantified. The minimum thickness of samples examined for GB properties contained GB and a few atomic layers around GB in order to predict thickness-independent properties of GB in ab initio simulations. In the continuum simulations, the thickness of the GB was set to be 2–8 nm based on the ab initio modeling work and experimental evidence. The brittleness index, defined as the ratio between the hardness and fracture toughness of the material, was chosen as the parameter of interest to compare the influence of different interfaces on fracture resistance contributions. The brittleness index is influenced by the GB strength as well as the temperature. The change in the thickness of GB did not significantly influence either the crack tip
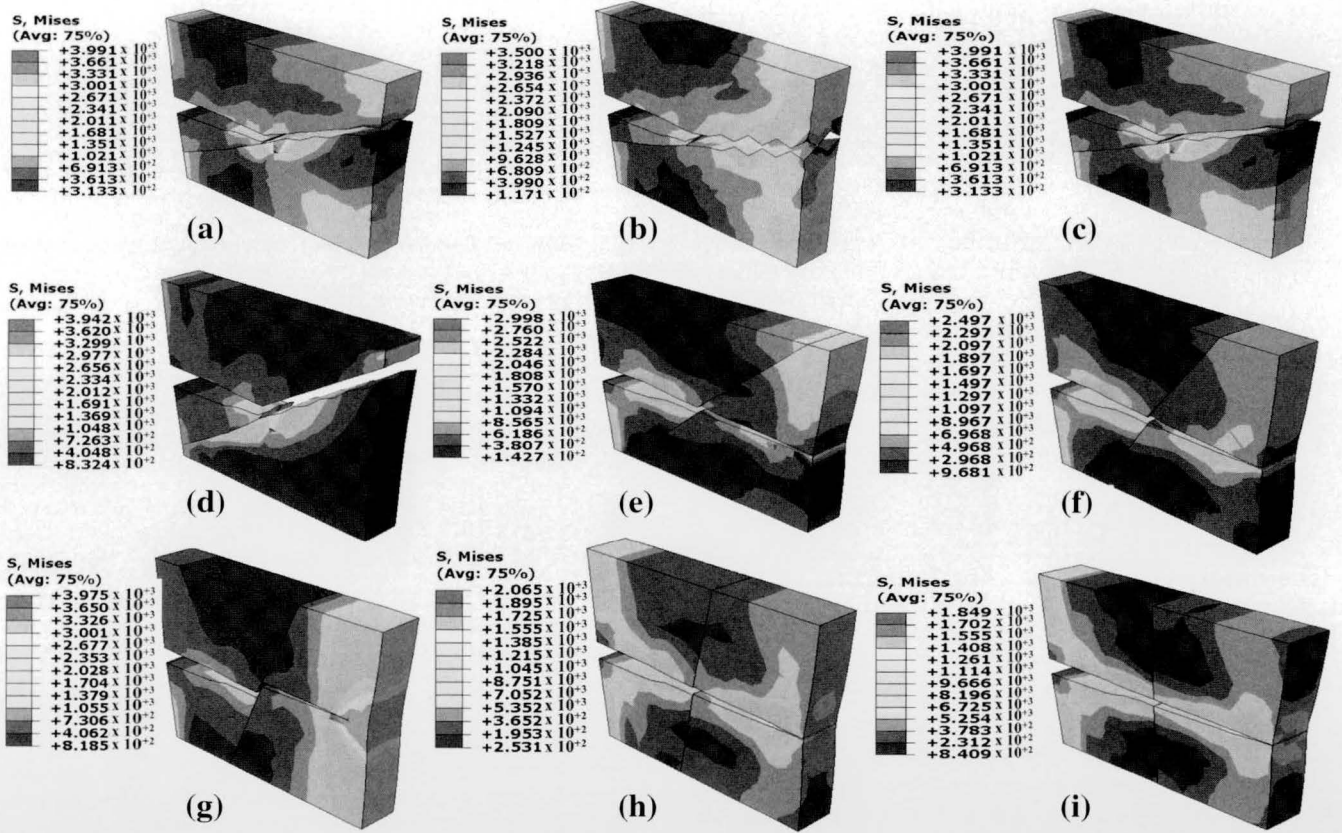
Fig. 4. Effect of GB angle with respect to advancing crack on the crack propagation path with orientation angle of (a) 10°, (b) 20°, (c) 30°, (d) 40°, (e) 50°, (f) 60°, (g) 70°, (h) 80°, and (i) 90°, for GB with maximum tensile strength T = 3600 MPa.

opening stresses (Fig. 3c and d) or crack tip energy dissipation, as shown in Fig. 3e, where all variations are in a very narrow zone of 4–5%. On the contrary, a small change in GB chemistry can significantly affect GB mechanical properties.

The obtained brittleness index of GBs in the current case was compared with the average brittleness index of grains in order to characterize the GB embrittlement caused by Ni addition. The brittleness index for the GB samples differed significantly from the grain brittleness index with the increase in Ni atomic wt.%, leading to an increase and then a decrease in the brittleness. The brittleness index parameter was found to have an inverse square root of length scale dependence Ref. 61 that can be expressed as $B = \alpha h^{-1/2}$, where h can be characterized as the characteristic size scale in the examined samples. The brittleness index is independent of the sample size and, therefore, needs to be defined accordingly. The length scale also needs to be extractable and applicable at multiple analyses size scales. Therefore, the size scale was taken as the characteristic crack length at GB. Parameter α is a coefficient for describing the weight of the length scale for a specific material. Using the proportionality factor $B = \alpha h^{-1/2}$, a modified brittleness index was introduced as

$$B^* = \frac{H}{K_c} \cdot \frac{1}{\alpha} \sqrt{h} \qquad (11)$$

The modified brittleness index is dimensionless with α found to be 3.3, as discussed in Ref. 59, so that the modified brittleness index for interface samples approaches the value of the average grain modified brittleness index. The revised brittleness index for the examined interface samples is shown in Fig. 3f. The revised values also closely corresponded to the experimental W microstructure values reported earlier by Evans and Wilshaw.[62] The impurities in the GB were suggested to be the main reason for the embrittlement effect of the GBs. The nickel percentages of 50–60% lead to the highest GB embrittlement effect matching the findings of the quantum mechanical calculations by Lee and Tomar.[9,10]

The effect of the orientation of the GB on the crack propagation direction was also analyzed. The orientation of the GB is related to the resolution of crack tip stresses along the GBs, and it determines the intergranular (crack advancing along the GB) or transgranular (crack passing through the GB) nature of failure. The GB angles of 0°–90° with respect to advancing cracks were analyzed. The

effect of different orientations of interfaces with respect to advancing cracks on the stress distribution in the material when the crack reaches the interface is shown in Fig. 4. Higher GB orientation angles with respect to advancing crack showed transgranular failure while lower GB angles lead to intergranular failure. These analyses also showed that there is a specific threshold GB angle that separates the intergranular and transgranular failure for a fixed GB maximum tensile strength. In the case of transgranular failure, deflection of the crack path appeared to be greater as the GB angle decreases. The greater deflection indicates the higher energy required for crack propagation. Intergranular failure and mixed mode failure occur for GB angles with respect to advancing cracks, varying in the range of $10°$–$40°$.

CONCLUSION

The interface plays a very important role in microstructural evolution during material processing as well as in material failure. The length scale of interfaces makes it extremely hard to extract their mechanical properties, such as hardness and fracture toughness, using experiments. Interface properties are also dependent on the chemical and physical configuration of the material system. PFM is shown to be an excellent tool to analyze and predict the evolution of the interfaces and the microstructure of materials during material processing. A combination of PFM with XFEM presents an excellent approach to combine interface property-dependent processing with interface property-dependent strength prediction for interface-based engineering of materials. In future, this study can be used to evaluate the applicability of a material in different operational conditions.

REFERENCES

1. S. Pal and M. Meraj, *Mater. Des.* 108, 168 (2016).
2. H. Yu, X. Zhou, W. Zhang, H. Peng, and C. Zhang, *Mater. Des.* 44, 320 (2013).
3. D. Verma, J. Singh, A.H. Varma, and V. Tomar, *JOM* 67, 1694 (2015).
4. D. Verma, T. Qu, and V. Tomar, *JOM* 67, 858 (2015).
5. T. Qu, D. Verma, M. Shahidi, B. Pichler, C. Hellmich, and V. Tomar, *MRS Bull.* 40, 349 (2015).
6. D. Verma and V. Tomar, *Mater. Sci. Eng., C* 44, 371 (2014).
7. I.J. Beyerlein, M.J. Demkowicz, A. Misra, and B.P. Uberuaga, *Prog. Mater Sci.* 74, 125 (2015).
8. T. Qu, D. Verma, M. Alucozai, and V. Tomar, *Acta Biomater.* 25, 325 (2015).
9. H. Lee and V. Tomar, *Comput. Mater. Sci.* 77, 131 (2013).
10. H. Lee and V. Tomar, *Int. J. Plast* 53, 135 (2014).
11. N.A. Mara, N. Li, A. Misra, and J. Wang, *JOM* 68, 143 (2016).
12. X. He and Y. Shen, *JOM* 67, 1486 (2015).
13. J. Wang, K. Kang, R.F. Zhang, S.J. Zheng, I.J. Beyerlein, and N.A. Mara, *JOM* 64, 1208 (2012).
14. N.A. Mara, I.J. Beyerlein, J.S. Carpenter, and J. Wang, *JOM* 64, 1218 (2012).
15. X. Zhang, E.G. Fu, A. Misra, and M.J. Demkowicz, *JOM* 62, 75 (2010).
16. L. Weng, Y. Shen, T. Fan, and J. Xu, *JOM* 67, 1499 (2015).
17. R. Srinivasan, R. Banerjee, G.B. Viswanathan, S. Nag, J.Y. Hwang, J. Tiley, and H.L. Fraser, *JOM* 62, 64 (2010).
18. J. Wang, C. Zhou, I.J. Beyerlein, and S. Shao, *JOM* 66, 102 (2014).
19. I.J. Beyerlein, N.A. Mara, J. Wang, J.S. Carpenter, S.J. Zheng, W.Z. Han, R.F. Zhang, K. Kang, T. Nizolek, and T.M. Pollock, *JOM* 64, 1192 (2012).
20. V.I. Dybkov, *JOM* 61, 76 (2009).
21. A. Gupta, S. Lee, R.B. Wagstaff, W. Mark Gallerneault, and J.W. Fenton, *JOM* 59, 62 (2007).
22. K.C. Jajam and H.V. Tippur, *Eng. Fract. Mech.* 78, 1289 (2011).
23. K.C. Jajam and H.V. Tippur, *Int. J. Solids Struct.* 49, 1127 (2012).
24. V.B. Chalivendra and A.J. Rosakis, *Eng. Fract. Mech.* 75, 2385 (2008).
25. Z.W. Shan, R.K. Mishra, S.A. Syed Asif, O.L. Warren, and A.M. Minor, *Nat. Mater.* 7, 115 (2008).
26. M.D. Uchic, D.M. Dimiduk, J.N. Florando, and W.D. Nix, *Science* 305, 986 (2004).
27. A. Kunz, S. Pathak, and J.R. Greer, *Acta Mater.* 59, 4416 (2011).
28. S.R. Kalidindi and S. Pathak, *Acta Mater.* 56, 3523 (2008).
29. S. Pathak, D. Stojakovic, R. Doherty, and S.R. Kalidindi, *J. Mater. Res.* 24, 1142 (2011).
30. R. Hahnlen and M.J. Dapino, *Compos. B* 59, 101 (2014).
31. B. Radhakrishnan, G.B. Sarma, and T. Zacharia, *Acta Mater.* 46, 4415 (1998).
32. S.Y. Hu and C.H. Henager Jr, *Acta Mater.* 58, 3230 (2010).
33. U. Grafe, B. Bottger, J. Tiaden, and S.G. Fries, *Model. Simul. Mater. Sci. Eng.* 8, 871 (2000).
34. I. Loginova, G. Amberg, and J. Agren, *Acta Mater.* 49, 573 (2001).
35. T. Uehara and T. Tsujino, *J. Cryst. Growth* 275, e219 (2005).
36. Y.M. Jin, A. Artemev, and A.G. Khachaturyan, *Acta Mater.* 49, 2309 (2001).
37. A. Yamanaka, T. Takaki, and Y. Tomita, *Mater. Sci. Eng., A* 491, 378 (2008).
38. S.Y. Hu and L.Q. Chen, *Acta Mater.* 49, 463 (2001).
39. D. Rodney, Y. Le Bouar, and A. Finel, *Acta Mater.* 51, 17 (2003).
40. S.Y. Hu, M.I. Baskes, and M. Stan, *Appl. Phys. Lett.* 90, 081921 (2007).
41. Y. Wang and J. Li, *Acta Mater.* 58, 1212 (2010).
42. A. Kazaryan, Y. Wang, S.A. Dregia, and B.R. Patton, *Phys. Rev. B* 61, 14275 (2000).
43. T. Uehara, T. Tsujino, and N. Ohno, *J. Cryst. Growth* 300, 530 (2007).
44. I.S. Aranson, V.A. Kalatsky, and V.M. Vinokur, *Phys. Rev. Lett.* 85, 118 (2000).
45. A. Karma, D.A. Kessler, and H. Levine, *Phys. Rev. Lett.* 87, 045501 (2001).
46. N. Moelans, B. Blanpain, and P. Wollants, *Calphad* 32, 268 (2008).
47. J.W. Cahn and J.E. Hilliard, *J. Chem. Phys.* 28, 258 (1958).
48. R.S. Qin and H.K. Bhadeshia, *Mater. Sci. Technol.* 26, 803 (2010).
49. Y.U. Wang, *Acta Mater.* 54, 953 (2006).
50. J.S. Lee, C. Minkwitz, and Ch. Herzig, *Phys. Status Solidi B* 202, 931 (1997).
51. J. Mundy, S. Rothman, N. Lam, H. Hoff, and L. Nowicki, *Phys. Rev. B* 18, 6566 (1978).
52. N.L. Peterson, *WAAD Technical report* (1960).
53. R.E. Pawel and T. Lundy, *Acta Metall.* 17, 979 (1969).
54. N. Arkhipova, S. Klotsman, Y.A. Rabovskij, and A. Timofeev, *Fiz. Met. Metalloved.* 43, 779 (1977).
55. G. Neumann and V. Tölle, *Philos. Mag. A* 61, 563 (1990).

56. S. Biswas, D. Schwen, J. Singh, and V. Tomar, *Extreme Mech. Lett.* 7, 78 (2016).

57. H. Lee and V. Tomar, *ASME J. Eng. Mater. Technol.* 134, 031010 (2012).

58. V.K. Gupta, D.-H. Yoon, H.M. Meyer Iii, and J. Luo, *Acta Mater.* 55, 3131 (2007).

59. C. Prakash, H. Lee, M. Alucozai, and V. Tomar, *Int. J. Fract.* 199, 1 (2016).

60. Abaqus, *Version 6.14 Documentation*. (Dassault Systemes Simulia Corp, Providence, 2014).

61. B.R. Lawn and D.B. Marshall, *J. Am. Ceram. Soc.* 62, 347 (1979).

62. A.G. Evans and T.R. Wilshaw, *Acta Metall.* 24, 939 (1976).